HAMOR, T. A., STEINFINK, H. & WILLIS, B. T. M. (1985). *Acta Cryst.* C**41**, 301-303.
HENDRICKSON, W. A. (1985). In *Methods in Enzymology*, Vol. 115. *Diffraction Methods for Biological Macromolecules, Part B*, edited by H. W. WYKOFF, C. H. W. HIRS & S. N. TIMASHEFF, pp. 252-270. New York: Academic Press.
HENDRICKSON, W. A. & KONNERT, J. H. (1980). In *Computing in Crystallography*, edited by R. DIAMOND, S. RAMASESHAN & D. VENKATESAN, pp. 13.01-13.26. Bangalore: Indian Academy of Sciences.
HILL, R. J. & FLACK, H. D. (1987). *J. Appl. Cryst.* **20**, 356-361.
HIRSHFELD, F. L. (1977). *Isr. J. Chem.* **16**, 226-229.
HIRSHFELD, F. L. & RABINOVICH, D. (1973). *Acta Cryst.* A**29**, 510-513.
IBERS, J. A. (1967). *Acta Cryst.* **22**, 604-605.
International Tables for Crystallography (1983). Vol. A, pp. 780-785. Dordrecht: Reidel. (Present distributor Kluwer Academic Publishers, Dordrecht.)
JAYNES, E. T. (1983). In *Papers on Probability, Statistics and Statistical Physics*, edited by R. O. ROSENKRANTZ, pp. 116-130. Dordrecht: Reidel (Present distributor Kluwer Academic Publishers, Dordrecht.)
JOHNSON, C. K. & LEVY, H. A. (1974). *International Tables for X-ray Crystallography*, Vol. IV, pp. 314-319. Birmingham: Kynoch Press. (Present distributor Kluwer Academic Publishers, Dordrecht.)
KENDALL, M. G. & STUART, A. (1979). *The Advanced Theory of Statistics*, Vol. 2, 4th ed. London: Griffin.
KUHS, W. F. (1983). *Acta Cryst.* A**39**, 148-158.
MANDEL, J. (1980). In *Accuracy in Powder Diffraction*, edited by S. BLOCK & C. HUBBARD, pp. 353-359. Washington, DC: US Government Printing Office.
MARSH, R. E. (1981). *Acta Cryst.* B**37**, 1985-1988.
MARSH, R. E. (1986). *Acta Cryst.* B**42**, 193-198.
MITRA, G. B., AHMED, R. & DAS GUPTA, P. (1985). In *Structure and Statistics in Crystallography*, edited by A. J. C. WILSON, pp. 151-181. Guilderland, NY: Adenine Press.
MORINO, Y., KUCHITSU, K. & MURATA, Y. (1965). *Acta Cryst.* **18**, 549-557.
MURATA, Y. & MORINO, Y. (1966). *Acta Cryst.* **20**, 605-609.
NICHOLSON, W. L., PRINCE, E., BUCHANAN, J. & TUCKER, P. (1982). In *Crystallographic Statistics*, edited by S. RAMASESHAN, M. F. RICHARDSON & A. J. C. WILSON, pp. 229-263. Bangalore: Indian Academy of Sciences.
PARRISH, W. (1960). *Acta Cryst.* **13**, 838-850.
PRINCE, E. (1982). *Mathematical Techniques in Crystallography and Materials Science*. New York: Springer.
PRINCE, E. (1985). In *Structure and Statistics in Crystallography*, edited by A. J. C. WILSON, pp. 95-103, 107. Guilderland, NY: Adenine Press.
PRINCE, E. (1989). *International Tables for Crystallography*, Vol. C. In preparation.
PRINCE, E. & NICHOLSON, W. L. (1985). In *Structure and Statistics in Crystallography*, edited by A. J. C. WILSON, pp. 183-195. Guilderland, NY: Adenine Press.
ROGERS, D. (1981). *Acta Cryst.* A**37**, 734-741.
ROLLETT, J. S. (1985). In *Structure and Statistics in Crystallography*, edited by A. J. C. WILSON, pp. 105-107. Guilderland, NY: Adenine Press.
ROLLETT, J. S. (1988). *Crystallographic Computing* 4: *New Techniques and New Technologies*, edited by N. W. ISAACS & M. R. TAYLOR, pp. 149-166. Oxford Univ. Press/International Union of Crystallography.
SEILER, P., SCHWEIZER, W. B. & DUNITZ, J. D. (1984). *Acta Cryst.* B**40**, 319-327.
SHMUELI, U. & KALDOR, U. (1981). *Acta Cryst.* A**37**, 76-80.
SHMUELI, U. & KALDOR, U. (1983). *Acta Cryst.* A**39**, 615-621.
SHMUELI, U. & WEISS, G. H. (1987). *Acta Cryst.* A**43**, 93-98.
SHMUELI, U. & WEISS, G. H. (1988). *Acta Cryst.* A**44**, 413-417.
SHMUELI, U., WEISS, G. H. & KIEFER, J. E. (1985). *Acta Cryst.* A**41**, 55-59.
SHMUELI, U., WEISS, G. H., KIEFER, J. E. & WILSON, A. J. C. (1984). *Acta Cryst.* A**40**, 651-660.
SHMUELI, U. & WILSON, A. J. C. (1981). *Acta Cryst.* A**37**, 342-353.
STEWART, R. F. (1976). *Acta Cryst.* A**32**, 565-574.
TAYLOR, R. & KENNARD, O. (1986). *Acta Cryst.* B**42**, 112-120.
THEIL, H. & NAGAR, A. L. (1961). *J. Am. Stat. Assoc.* **56**, 793-806.
TUKEY, J. W. (1974). In *Critical Evaluation of Chemical and Physical Structural Information*, edited by D. R. LIDE & A. P. MARTIN, pp. 3-14, 48-58. Washington, DC: National Academy of Sciences.
WANG, H., BARTON, R. J. & ROBERTSON, B. E. (1986). *Program Abstracts. Am. Crystallog. Assoc. Annu. Meet.*, Hamilton, Ontario, Ser. 2, Vol. 14, p. 23. American Crystallographic Association.
WANG, H. & ROBERTSON, B. E. (1985). In *Structure and Statistics in Crystallography*, edited by A. J. C. WILSON, pp. 125-135. Guilderland, NY: Adenine Press.
WASER, J. (1963). *Acta Cryst.* **16**, 1091-1094.
WILSON, A. J. C. (1949). *Acta Cryst.* **2**, 318-321.
WILSON, A. J. C. (1976*a*). *Acta Cryst.* A**32**, 781-783.
WILSON, A. J. C. (1976*b*). *Acta Cryst.* A**32**, 994-996.
WILSON, A. J. C. (1979). *Acta Cryst.* A**35**, 122-130.
WILSON, A. J. C. (1980*a*). *Acta Cryst.* A**36**, 929-936.
WILSON, A. J. C. (1980*b*). *Acta Cryst.* A**36**, 937-944.

Acta Cryst. (1989). A**45**, 75-85

Two-Dimensional Intensity Distributions Obtained with Crystal-Monochromated X-radiation and a Small Specimen Crystal

BY ANDREW W. STEVENSON

Division of Materials Science and Technology, CSIRO, Locked Bag 33, *Clayton, Victoria, Australia* 3168

(*Received* 29 *February* 1988: *accepted* 21 *July* 1988)

Abstract

Two-dimensional ($\Delta\omega$, $\Delta 2\theta$) intensity distributions in the plane of diffraction are calculated for the case of crystal-monochromated X-radiation incident on a small specimen. The calculations are based on ray tracing and take into account the mosaic spread of the monochromator, depth of penetration into the monochromator, source emissivity distribution, wavelength distribution, broadening due to the

0108-7673/89/010075-11$03.00

detector aperture, and various aspects of the experimental arrangement involved. The general form of the $\Delta\omega$, $\Delta 2\theta$ distributions for the case of a monochromator and small specimen crystal is considered. Some calculations are compared with experimental results and reveal excellent agreement.

1. Introduction

The development of the two-dimensional $\Delta\omega, \Delta 2\theta$ measurement technique (Mathieson, 1982) has pointed to a number of advantages in comparison with the conventional one-dimensional profile technique. The $\Delta\omega, \Delta 2\theta$ technique results in a form of partial deconvolution for the various components present (specimen mosaic spread μ_S, monochromator mosaic spread μ_M, source emissivity σ, wavelength distribution λ, specimen-crystal size c, and detector aperture δ). In this way the technique is capable of revealing subtleties present in the individual components, which might normally be overlooked (*e.g.* Mathieson & Stevenson, 1984, 1985, 1986*a*; Stevenson, Mathieson & White, 1986; Wilkins, Chadderton & Smith, 1983).

The $\Delta\omega, \Delta 2\theta$ measurement technique has also indicated ways in which the conventional integrated X-ray intensity measurement procedure can be improved (*e.g.* Mathieson, 1983, 1984*a*,*b*). These improvements are essentially ways of ensuring that reflections are truncated in a more consistent manner over the full range of specimen-crystal Bragg angle θ_S, the result being greater structure-factor accuracy (*e.g.* Mathieson, 1984*c*).

Mathieson (1985*a*,*b*,*c*) has considered, theoretically, the case where a crystal monochromator M is included in the experimental arrangement, from the $\Delta\omega, \Delta 2\theta$ point of view. Mathieson (1985*a*) has investigated the effects that the mosaic spread of the monochromator, the depth of penetration into the monochromator and the wavelength band have in this context. The focus of attention is the interaction of the wavelength dispersion of the monochromator and that of the small specimen, S. Mathieson (1988*b*) has recently reconsidered the inclusion of a monochromator in the experimental set-up, giving rise to some small changes in comparison with Mathieson (1985*a*).

The aim of the present study is to calculate the intensity distribution in $\Delta\omega, \Delta 2\theta$ space [we refer, throughout this paper, to the ω-scan mode - the results for other scan modes can easily be obtained by using affine transformations (see, for example, Mathieson & Stevenson, 1985)] for the experimental arrangement of an X-ray source, a flat monochromator M, a small specimen S, and a detector with a narrow aperture in front of it (or a linear position-sensitive detector). Rather than convoluting the functions associated with the various components together in $\Delta\omega, \Delta 2\theta$ space [a procedure that has been used successfully in the non-monochromator case - see Stevenson (1989)], a ray-tracing analysis has been used. Such calculations avoid making certain assumptions which may not be justifiable here (see also Mathieson, 1988*b*). The success of the calculations can be judged by the agreement with certain experimental $\Delta\omega, \Delta 2\theta$ distributions. The calculations also suggest other experimental tests which might be carried out.

This work is relevant not only to laboratory X-ray sources, but also to diffraction with synchrotron sources (see also Mathieson, 1988*a*), neutrons and γ-rays, since the form of the individual functions involved (for example, μ_M, σ, λ and δ) are readily changed. Mathieson (1988*b*) is, in particular, concerned with the neutron case.

2. Theory

We consider the experimental arrangement to be as depicted schematically in Fig. 1. The situation shown, which defines the origin of $\Delta\omega, \Delta 2\theta$ space, has X-radiation of wavelength λ_0 emanating from the 'centre' ($x = 0$) of the source, diffracting from the surface of the monochromator (and involving a mosaic orientation $\Delta = 0°$) at its centre ($y = 0$) with Bragg angle θ_M, then diffracting again, from a point specimen with Bragg angle θ_S, and entering the detector *via* a narrow aperture (slit). The second diffraction process can occur, relative to the first, in one of two senses. The $(+, -)$ setting involves the monochromator and specimen rotation axes being 'in opposite senses' and the $(+, +)$ setting involves them being 'in the same sense', the cases of $\theta_S = \theta_M$ being the classical $(n, -n)$ and (n, n) settings of the two-crystal spectrometer respectively (see Compton & Allison, 1935; Mathieson, 1968). We denote the path lengths in Fig. 1, source to monochromator, monochromator to specimen and specimen to detector slit, by d_1, d_2 and d_3 respectively.

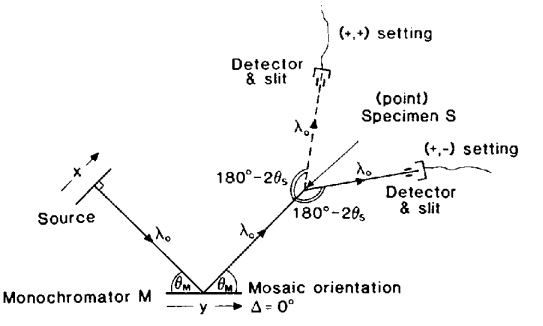

Fig. 1. Schematic diagram of the experimental arrangement.

Source

We assume that each point on the source can emit all wavelengths (wavelength distribution λ) in any relevant direction with source emissivity distribution σ. The width of the projected focal spot in the diffraction plane is denoted w_1.

Monochromator

The monochromator is assumed to be planar and often (though not necessarily*) effectively infinite in extent along y. The thickness of the monochromator, perpendicular to the face, is denoted w_2. The monochromator mosaic spread μ_M is assumed to be homogeneous throughout. The Bragg planes (for $\Delta = 0°$) are assumed to be parallel to the monochromator face.

Specimen

In the present study we treat the case of a point specimen which is perfect. The use of small but finite crystals (and those which are only 'nearly perfect') does not invalidate the following treatment. The case of large and/or imperfect specimen crystals would require some modifications, however. These assumptions mean that μ_S and c can be treated as delta functions in this analysis.

Detector/slit

The slit should be narrow in the diffraction plane (subtending an angle of the order of a few minutes at the specimen crystal), and is placed directly in front of the detector. The functional form of the detector-aperture distribution δ is rectangular and of an angular width equal to that subtended by the slit (width w_3) at S, *i.e.* $180°w_3/(d_3\pi)$.

The interplanar spacings of the monochromator and specimen are d_M and d_S respectively, and so $\lambda_0 = 2d_S \sin\theta_S = 2d_M \sin\theta_M$.

Initially, we will assume that there is no depth of penetration into the monochromator. By considering a singly diffracted beam from a general position y on M and going through S, it is a simple matter to show that the (acute) angle between the beam and the monochromator face (in the diffraction plane) is given by

$$\beta = \tan^{-1}\left(\frac{d_2 \sin\theta_M}{d_2 \cos\theta_M - y}\right). \tag{1}$$

At this stage we cannot determine the wavelength λ involved in this singly diffracted beam since the mosaic orientation Δ is unknown. Both λ and Δ will be fixed when the position x on the source is specified.

* If M is finite along y we assume that no radiation can pass through the sides (thickness w_2).

By considering a beam emanating from a general position x on the source and going to position y on M, it can be shown that the (acute) angle between the beam and the monochromator face is given by

$$\alpha = \tan^{-1}[p \sin\gamma/(y - p\cos\gamma)], \tag{2a}$$

where

$$p = (x^2 + d_1^2)^{1/2} \tag{2b}$$

and

$$\gamma = 180° - \theta_M - \tan^{-1}(x/d_1). \tag{2c}$$

The mosaic orientation involved in the (first) diffraction process is then given as

$$\Delta = (\alpha - \beta)/2. \tag{3}$$

The wavelength involved is given by

$$\lambda = 2d_M \sin[(\alpha + \beta)/2]. \tag{4}$$

For the case depicted in Fig. 1 $\alpha = \beta = \theta_M$, so that (3) and (4) give $\Delta = 0°$ and $\lambda = \lambda_0$ respectively.

Using (1)-(4), we find that particular values of x and y lead to unique values of Δ and λ. For the $(+, -)$ setting we consider clockwise rotations of the specimen and the detector to be positive $\Delta\omega$ and $\Delta 2\theta$ respectively. For the $(+, +)$ setting we consider anticlockwise rotations to be positive $\Delta\omega$ and $\Delta 2\theta$. The Bragg condition for the specimen crystal implies

$$\lambda = 2d_S \sin(\theta_S \mp \beta \pm \theta_M + \Delta\omega), \tag{5}$$

where the lower sign applies to the $(+, -)$ setting and the upper sign to the $(+, +)$ setting. Using (4) and (5) we get

$$\Delta\omega = \sin^{-1}\{d_M \sin[(\alpha + \beta)/2]/d_S\} - \theta_S \pm \beta \mp \theta_M, \tag{6}$$

and it can be shown that

$$\Delta 2\theta = 2\Delta\omega \mp \beta \pm \theta_M. \tag{7}$$

Equations (6) and (7) can be shown to be consistent with equations (1)-(3a) of Mathieson (1985a). From (7)

$$\beta = \pm 2\Delta\omega \mp \Delta 2\theta + \theta_M, \tag{8}$$

and using (1) we get

$$y = d_2 \cos\theta_M - d_2 \sin\theta_M / \tan(\pm 2\Delta\omega \mp \Delta 2\theta + \theta_M). \tag{9}$$

Equations (6) and (7) imply

$$\alpha = 2\sin^{-1}[d_S \sin(\Delta 2\theta - \Delta\omega + \theta_S)/d_M] \mp 2\Delta\omega \pm \Delta 2\theta - \theta_M. \tag{10}$$

Using (2a) and the geometrical conditions

$$p \sin\gamma = d_1 \sin\theta_M + x \cos\theta_M \tag{11a}$$

and

$$p \cos\gamma = x \sin\theta_M - d_1 \cos\theta_M, \tag{11b}$$

we obtain the result

$$x = \frac{y \tan \alpha + d_1(\cos \theta_M \tan \alpha - \sin \theta_M)}{\cos \theta_M + \sin \theta_M \tan \alpha}, \quad (12)$$

where α is given by (10).

It is now possible to calculate, for a given point in $\Delta\omega, \Delta 2\theta$ space, the corresponding position on the monochromator face (in the diffraction plane) y [from (9)] and the corresponding position on the source x [from (10) and (12)]. The values of α and β can be used to calculate the values of Δ and λ [from (3) and (4) respectively]. The 'intensity' for the given $\Delta\omega, \Delta 2\theta$ point is then calculated as the product of the values of the functions associated with $\mu_M(\Delta)$, $\sigma(x)$ and $\lambda(\lambda)$. In the event that the value of $x(y)$ does not correspond to a position on the source (monochromator), the 'intensity' for the given $\Delta\omega, \Delta 2\theta$ point is zero.

In order to take account of the broadening in the $\Delta 2\theta$ direction, caused by the detector aperture (slit of width w_3), the calculated $\Delta\omega, \Delta 2\theta$ intensity distribution can be numerically convoluted with δ, of a form described in the previous section.

3. Aspects of the $\Delta\omega, \Delta 2\theta$ distribution

From (5) and (8),

$$\lambda = 2d_S \sin(\theta_S - \Delta\omega + \Delta 2\theta) \quad (13)$$

which implies that the wavelength is constant along lines of gradient 1 in $\Delta\omega, \Delta 2\theta$ space ($\lambda = \lambda_0$ along $\Delta\omega = \Delta 2\theta$).

From (9) we see that the associated position along the face of the monochromator (in the diffraction plane) is constant along lines of gradient 1/2 in $\Delta\omega, \Delta 2\theta$ space ($y = 0$ along $\Delta\omega = \Delta 2\theta/2$).

Using (3), (8) and (10), we obtain

$$\Delta \simeq (d_S \cos \theta_S / d_M \cos \theta_M)(\Delta 2\theta - \Delta\omega) \mp 2\Delta\omega \pm \Delta 2\theta, \quad (14)$$

from which we get

$$\Delta\omega = \Delta 2\theta\left(\frac{t \pm 1}{2t \pm 1}\right) \mp \frac{t\Delta}{2t \pm 1}, \quad (15)$$

where $t = \tan \theta_S / \tan \theta_M$.* The approximations made in deriving (14) were that $\sin \varepsilon \simeq \varepsilon$ and $\cos \varepsilon \simeq 1$ for small ε. The mosaic orientation involved is constant along lines of gradient $(t \pm 1)/(2t \pm 1)$ in $\Delta\omega, \Delta 2\theta$ space [$\Delta = 0$ along $\Delta\omega = \Delta 2\theta(t \pm 1)/(2t \pm 1)$] ($t \neq 0$).

Mathieson (1988*b*) has briefly discussed the shape of reflections in $\Delta\omega, \Delta 2\theta$ space for the case of a near-parallel incident beam (small divergence in the diffraction plane). A parallel incident beam corresponds, in the present case, to the rather severe restriction that α can only have the value θ_M. Such a situation is approximated, for example, at synchrotron radiation sources, where the beam divergence is, say, 20″ (see also Mathieson, 1988*a*). From (10) it can be shown that $\alpha = \theta_M$ implies $\Delta\omega \simeq \Delta 2\theta(t \pm 2)/(2t \pm 2)$ [$\Delta 2\theta \simeq 0$ for $t = 1{\cdot}0$ in the (+, −) setting]. Thus the $\Delta\omega, \Delta 2\theta$ distribution for such a case is a line of gradient $(t \pm 2)/(2t \pm 2)$ through the origin. In particular, for $t = 1{\cdot}0$ ($2{\cdot}0$) in the (+, −) setting the line is parallel to the $\Delta\omega$ ($\Delta 2\theta$) axis. Various other simplifications occur when $\alpha = \theta_M$, *e.g.* (12) will reduce to $x = y \sin \theta_M$ and (14) becomes $\Delta \simeq -\Delta 2\theta/(2t \pm 2)$ [$\Delta \simeq \Delta\omega$ for $t = 1{\cdot}0$ in the (+, −) setting].

From (9), (10) and (12), and using the above-mentioned small-angle approximations, we find

$$x \simeq \{d_1[2(\Delta 2\theta - \Delta\omega)/t \mp (2\Delta\omega - \Delta 2\theta)] \times \tan \theta_M \pm d_2(2\Delta\omega - \Delta 2\theta) \tan \theta_M\} \times \{\tan \theta_M \pm (2\Delta\omega - \Delta 2\theta)\}^{-1} \quad (16)$$

and therefore

$$\Delta\omega = \{\pm x + \tan \theta_M[2d_1/t \pm (d_1 - d_2)]\}\Delta 2\theta \times \{\pm 2x + \tan \theta_M[2d_1/t \pm 2(d_1 - d_2)]\}^{-1} - (x \tan \theta_M) \times \{\pm 2x + \tan \theta_M[2d_1/t \pm 2(d_1 - d_2)]\}^{-1}. \quad (17)$$

For the trivial case of $t = 0$ ($\theta_S = 0$) (17) reduces to $\Delta\omega = \Delta 2\theta$ (for any value of x), as does (13) (for any value of λ) and (15) (for any value of Δ). In instances where θ_S is considerably larger than θ_M (as might be the case, for example, with a pyrolytic graphite 002 reflection for monochromation), so that $2d_1/t \ll |d_1 - d_2|$ (for suitable d_1 and d_2), (17) implies that the source position is constant along lines of approximate gradient 1/2 in $\Delta\omega, \Delta 2\theta$ space. In cases where $d_1 = d_2$ (and x is small compared with d_1) (17) implies that the source position is constant along lines of approximate gradient 1 in $\Delta\omega, \Delta 2\theta$ space. In general, the line in $\Delta\omega, \Delta 2\theta$ space corresponding to $x = 0$ has gradient $[2d_1/t \pm (d_1 - d_2)]/[2d_1/t \pm 2(d_1 - d_2)]$ and goes through the origin ($t \neq 0$).

In order to demonstrate some of the aspects of the $\Delta\omega, \Delta 2\theta$ distribution mentioned above, Fig. 2 displays the calculated results for μ_M, σ and λ of rectangular shape [except that in (*a*), μ_M is triangular, in (*b*), σ is triangular, and in (*c*), λ is triangular] with base widths 0·4°, 0·8 mm and 0·02 Å respectively. In addition, these functional forms are symmetric about $\Delta = 0$, $x = 0$ and $\lambda = \lambda_0$, respectively. For these calculations, $d_1 = 10$, $d_2 = 1$ cm, $\theta_M = 30°$, $\lambda_0 = 1$ Å, the detector slit is assumed to be of negligible width ($w_3/d_3 \simeq 0$), depth of penetration into the monochromator is ignored and the monochromator

* For the special case of $t = 0{\cdot}5$ in the (+, −) setting (15) is replaced by $\Delta 2\theta = \Delta$, *i.e.* the mosaic orientation involved is constant along lines parallel to the $\Delta\omega$ (vertical) axis.

is assumed to be infinite in extent along y. Parts (i) to (vi) of Fig. 2 correspond to $t = 0{\cdot}25$, $0{\cdot}5$, $0{\cdot}75$, $1{\cdot}0$, $1{\cdot}25$ and $1{\cdot}5$, for the $(+, -)$ setting.

Fig. 2 displays the dramatic change in shape and size of the two-dimensional intensity distribution as a function of t. This indicates that for conventional one-dimensional intensity-profile determination both the scan range and detector-aperture size should be varied as a function of t (θ_S, for fixed θ_M) for consistent truncation of reflections (see Mathieson, 1985*a*,*b*,*c*). The intensity distributions in Fig. 2 are bounded by a pair of lines along the direction of constant Δ [see (15)] and a pair of lines along the direction of constant x [see (17); in the cases considered, the value of x has a negligible effect on the value of the coefficient of $\Delta 2\theta$]. Thus for the case of $t = 0{\cdot}5$ $(1{\cdot}0)$ two of the sides of the resulting parallelogram are parallel to $\Delta\omega$ $(\Delta 2\theta)$ [see (15)]. As $t \to 0$ the distributions in Fig. 2 tend to a line of gradient 1 in $\Delta\omega$, $\Delta 2\theta$ space (as already discussed).

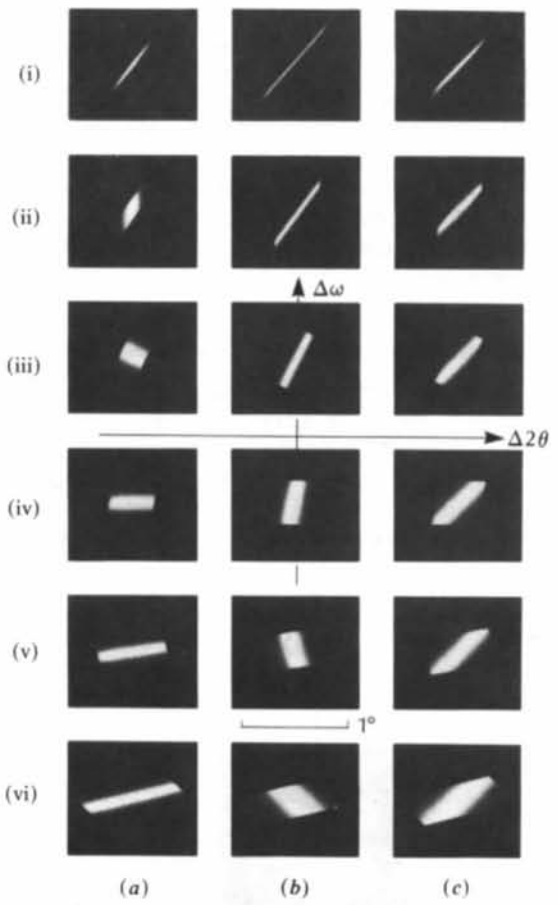

Fig. 2. Calculated $\Delta\omega$, $\Delta 2\theta$ intensity distributions for (*a*) triangular μ_M, rectangular σ and λ; (*b*) triangular σ, rectangular μ_M and λ; (*c*) triangular λ, rectangular μ_M and σ. The base widths of μ_M, σ and λ are 0·4°, 0·8 mm and 0·02 Å respectively. The respective functional forms are symmetric about $\Delta = 0$, $x = 0$ and $\lambda = \lambda_0$. Other relevant parameter values are given in the text. The values of θ_S, for the $(+, -)$ setting, are such that t takes the values (i) 0·25, (ii) 0·5, (iii) 0·75, (iv) 1·0, (v) 1·25 and (vi) 1·5.

In Figs. 2(*a*) (i) to (vi) we see the way the direction of constant Δ changes, as predicted by (15). The cases of $t = 0{\cdot}5$ and $1{\cdot}0$ are particularly noteworthy (see above), with the latter corresponding to the classical $(n, -n)$ setting of the double-crystal spectrometer. Figs. 2(*b*) (i) to (vi) show the change in the direction for constant x, in accord with (17). Finally, Figs. 2(*c*) (i) to (vi) show the direction of constant λ to be at 45° to the $\Delta\omega$ and $\Delta 2\theta$ axes, as predicted by (13), regardless of t. As t becomes large, it can be seen from (15) and (17) that the gradients for the directions of constant Δ and x will both approach 1/2.

The calculations presented in Fig. 2 are restricted to the $(+, -)$ setting. Similar calculations for the $(+, +)$ setting are quite straightforward, but do not offer any especially new insights. In fact, these two-dimensional distributions do not show the remarkable variation seen in Fig. 2, largely because $(t-1)/(2t-1)$ changes from 1 to ∞ and then from $-\infty$ to 0 to 0·5, as t changes from 0 to ∞, whereas $(t+1)/(2t+1)$ only changes from 1 to 0·5.

The boundary of the two-dimensional intensity distributions is dependent on the interaction of several factors in the experimental arrangement including incident-beam geometry, source size, monochromator size, monochromator mosaic spread, wavelength band, and so on. In order to demonstrate this point we will examine the distribution for $t = 0{\cdot}75$ in Fig. 2, this time, for convenience, with μ_M, σ and λ all represented by rectangular functional forms. Fig. 3 shows the calculated two-dimensional intensity distributions for $t = 0{\cdot}75$, with the same parameter values as for Fig. 2, but with the monochromator size (along y) restricted to (*a*) 0·4, (*b*) 0·3, (*c*) 0·2, (*d*) 0·1 and (*e*) 0·04 mm (symmetrically about $y = 0$). Fig. 4 shows the calculated two-dimensional intensity distributions for $t = 0{\cdot}75$, with the same parameter values as for Fig. 2, but with a monochromator size of 0·4 mm and a source size (w_1) of (*a*) 2·4, (*b*) 1·6, (*c*) 1·2, (*d*) 0·8, (*e*) 0·4 and (*f*) 0·2 mm. For the calculations in Fig. 2 the monochromator was assumed to be infinite in

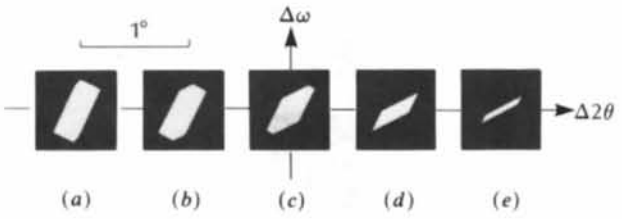

Fig. 3. Calculated $\Delta\omega$, $\Delta 2\theta$ intensity distributions for $t = 0{\cdot}75$, with the same parameter values as for Fig. 2, but μ_M, σ and λ are all rectangular functional forms, and the monochromator size (along y) has been restricted to (*a*) 0·4, (*b*) 0·3, (*c*) 0·2, (*d*) 0·1 and (*e*) 0·04 mm (symmetrically about $y = 0$).

extent along y. In fact, only values of y in the interval $(-0{\cdot}187,\ 0{\cdot}183)$ mm were necessary, *i.e.* a monochromator size of, say, 0·4 mm [as in Fig. 3(a)] or larger could have been considered to be infinite. The monochromator size for Fig. 4 is also effectively infinite. Figs. 3(a) and 4(d) are both the same as Figs. 2(a)(iii), 2(b)(iii) and 2(c)(iii) would be if the triangular functional form in each were replaced by the rectangle. It is therefore pertinent to note that a third pair of lines, at 45° to the $\Delta\omega$ and $\Delta 2\theta$ axes, also forms a small part of the boundary of this two-dimensional distribution. This effect is not evident in Fig. 2 (for any value of t). This third pair of lines is along the direction of constant λ [see (13)].

In Fig. 3 we see the effect of making the monochromator smaller (along y), in that a pair of lines at $\tan^{-1}(1/2)$ to the $\Delta 2\theta$ (horizontal) axis increasingly truncates the $\Delta\omega, \Delta 2\theta$ distributions [no such truncation occurs in Fig. 3(a)]. In Fig. 4 we see the effect of making the source smaller (along x), in that a pair of lines at approximately 64° to the $\Delta 2\theta$ axis increasingly truncates the $\Delta\omega, \Delta 2\theta$ distributions [no such truncation occurs in Fig. 4(a)]. The significance of the angle 64° in this case is that it represents $\tan^{-1}\{[2d_1/t-(d_1-d_2)]/[2d_1/t-2(d_1-d_2)]\}$, as discussed in connection with (17).

In certain circumstances the two-dimensional intensity distribution under consideration might be bounded by four pairs of lines, these representing limitations on μ_M, σ, λ and the monochromator size. For example, Fig. 5 shows the calculated $\Delta\omega, \Delta 2\theta$ distribution for $t=0{\cdot}75$, with the same parameter values as for Fig. 2, but with a monochromator size of 0·26 mm and a source size of 1·5 mm.

It should be pointed out that there is a definite 'sense' to the way in which μ_M, σ and λ occur in the $\Delta\omega, \Delta 2\theta$ distributions. So far we have considered only symmetric functional forms, but if a particular component is asymmetric, the resulting two-dimensional intensity distributions show this in a predictable manner. This point will be borne out in § 5, where μ_M shows some effects akin to fragmentation and λ is double peaked (representing a $K\alpha$ doublet).

The functional forms used in this section, especially those for μ_M and λ, may not be considered very realistic; however, the use of such functions is most helpful in ascertaining the basic features of the two-dimensional intensity distributions. Having gained initial insight with such an analysis, one is then better equipped to handle the more realistic situations of, say, Gaussians and Lorentzians for μ_M and λ, and trapezoids for σ.

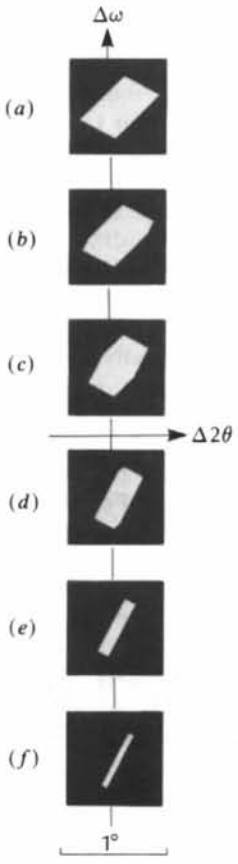

Fig. 4. Calculated $\Delta\omega, \Delta 2\theta$ intensity distributions for $t=0{\cdot}75$, with a monochromator size of 0·4 mm and a source size (w_1) of (a) 2·4, (b) 1·6, (c) 1·2, (d) 0·8, (e) 0·4 and (f) 0·2 mm.

4. Depth of penetration into the monochromator

The effect of depth of penetration into the monochromator cannot be ignored in the case of, for example, pyrolytic graphite (see Mathieson, 1985*a*). In order to take account of this effect in our calculation of two-dimensional intensity distributions we introduce another variable, z, which represents the

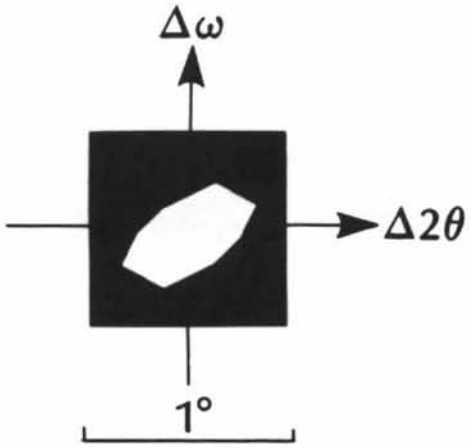

Fig. 5. Calculated $\Delta\omega, \Delta 2\theta$ intensity distribution for $t=0{\cdot}75$, with a monochromator size of 0·26 mm and a source size of 1·5 mm.

distance into the monochromator from the face, along the surface normal. The value of z at the monochromator surface is zero and the 'back' face w_2.

If we proceed in a similar manner to that outlined in § 2, (1), (2b) and (2c) still hold but (2a) becomes

$$\alpha = \tan^{-1}\left(\frac{y \sin\beta \sin\psi + p \sin\gamma \sin(\beta+\psi)}{y \sin\beta \cos\psi - p \cos\gamma \sin(\beta+\psi)}\right), \quad (18a)$$

where

$$\psi = \tan^{-1}[z/(y - z\cot\beta)]. \quad (18b)$$

The value of ψ should be in the first or second quadrant.

Equations (3)-(11b) still hold but (12) becomes

$$x = [y \sin\beta (\cos\psi \tan\alpha - \sin\psi) + d_1 \sin(\beta+\psi)(\cos\theta_M \tan\alpha - \sin\theta_M)] \times [\sin(\beta+\psi)(\cos\theta_M + \sin\theta_M \tan\alpha)]^{-1}. \quad (19)$$

If $z = 0$, (18b) implies $\psi = 0$ (or 180°), (18a) reduces to (2a) and (19) reduces to (12). If $y = 0$, (18b) implies $\psi = 180° - \beta$ ($= 180° - \theta_M$), (18a) is replaced by

$$\alpha = \tan^{-1}\left(\frac{z \sin\psi + p \sin\gamma \sin\beta}{z \cos\psi - p \cos\gamma \sin\beta}\right) \quad (20)$$

and (19) is replaced by

$$x = \frac{z \sin(\theta_M + \alpha) + d_1 \sin\theta_M \sin(\theta_M - \alpha)}{-\sin\theta_M \cos(\theta_M - \alpha)}. \quad (21)$$

If $z = 0$ and $y = 0$, (18b) is ignored, and (18a) and (19) are replaced by (2a) and (12) respectively.

For a given $\Delta\omega, \Delta 2\theta$ point α, β and y can be calculated as before and then Δ and λ, but there is no longer a unique value of x. The value of x depends on z and, for a given $\Delta\omega, \Delta 2\theta$ point, has the form $x = -Az + B$, where A and B are constants and $A > 0$. Thus the greater the depth of penetration, the further the corresponding source position is in the negative-x direction. The resulting 'intensity' for a given $\Delta\omega, \Delta 2\theta$ point is the product of $\mu_M(\Delta)$, $\lambda(\lambda)$, $\gamma(y)$ and η. The function $\gamma(y)$ is rectangular, being positive when y corresponds to a position on the monochromator face (for the outgoing beam) and zero otherwise. The function η can be represented as

$$\eta = \sum_{z=0}^{w_2} \gamma(y')\sigma(x) \exp[-z\chi(\alpha - \theta_M)/\sin\alpha] \times \exp[-z\chi(\beta - \theta_M)/\sin\beta], \quad (22)$$

where the first (second) exponential represents the attenuation factor for the incoming (outgoing) beam inside the monochromator. χ is an effective absorption coefficient, a function of the deviation from the Bragg angle (*e.g.* Calvert, Killean & Mathieson, 1976). It must be stressed that the value of x, on which $\sigma(x)$ depends, is itself dependent on z. $\gamma(y')$ appears in (22) to ensure that incoming beams pass through the monochromator face, where $y' = y - z(\cot\alpha + \cot\beta)$. The summation in (22) is carried out over N values, so that the increment in z is given by $\Delta z = w_2/(N-1)$, and $\Delta z \gg d_M$.

Fig. 6 is a schematic diagram of the depth-of-penetration situation for three values of α and β. We see that for the beams represented by dot-dash lines ($\alpha = \alpha'$ and $\beta = \beta'$) the source will not supply radiation for the larger depths of penetration, and so the intensity at the corresponding $\Delta\omega, \Delta 2\theta$ point will be somewhat diminished. For the solid lines ($\alpha = \alpha''$ and $\beta = \beta''$) the source does not present a limitation for any depth of penetration. In the case of the dashed lines ($\alpha = \alpha'''$ and $\beta = \beta'''$) the source will not supply radiation for the smaller depths of penetration, and the corresponding intensity in $\Delta\omega, \Delta 2\theta$ space will be severely reduced, because the beams from near the monochromator surface are those which suffer least attenuation (owing to smaller crystal path lengths).

The minimum source size necessary to satisfy all depths of penetration for a particular $\Delta\omega, \Delta 2\theta$ point is given by

$$x_{\min} = \frac{w_2 \sin(\alpha+\beta)}{\sin\beta \cos(\theta_M - \alpha)} \simeq 2w_2 \cos\theta_M, \quad (23)$$

assuming that this is correctly disposed in the diffraction plane, *i.e.* in the general case, the source of size $x_{\min}$ would not be centred on $x = 0$. In carrying out simulations of experimental $\Delta\omega, \Delta 2\theta$ intensity distributions where the depth-of-penetration effect is important and w_1 is relatively small, the position of the source along the line of x will need to be well defined, and may be quite 'lop-sided' with respect to $x = 0$ (as defined in Fig. 1). A useful test in this regard might be, for example, the agreement of observed and calculated $K\alpha_1$-to-$K\alpha_2$ intensity ratios in $\Delta\omega, \Delta 2\theta$ space.

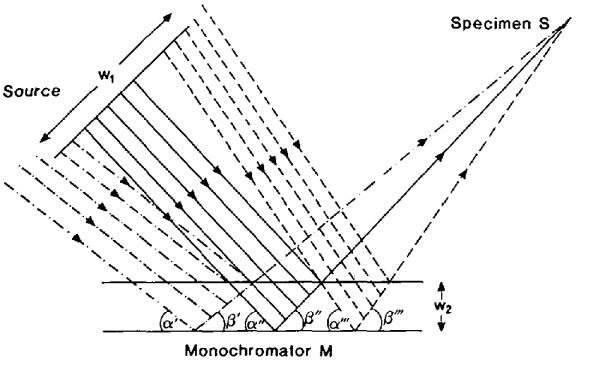

Fig. 6. Schematic diagram of the depth-of-penetration situation for three values of α and β.

Fig. 7 shows the calculated $\Delta\omega, \Delta 2\theta$ distributions for $t = 1{\cdot}0$, with the same parameter values as for Fig. 2 (μ_M, σ and λ all being of rectangular shape here), but with allowance for depth-of-penetration effects and w_2 equal to (*a*) 0·0, (*b*) 0·1, (*c*) 0·2, (*d*) 0·3, (*e*) 0·4 and (*f*) 3·0 mm. The value of Δz used in these calculations was 1 μm, and $\chi(\theta-\theta_M) = 2\exp[-16\ln 2(\theta-\theta_M)^2]+8\ \text{cm}^{-1}$ (with $\theta-\theta_M$ expressed in degrees), *i.e.* a Gaussian of height 2 cm^{-1} and FWHM 0·5° sitting on a base level of 8 cm^{-1}.

As the thickness of the monochromator (w_2) increases in Fig. 7 we can see a progressive increase in the intensity at points of higher $\Delta 2\theta$, up to a limit imposed by λ (a line at 45° to the $\Delta\omega$ and $\Delta 2\theta$ axes). This effect can be understood from Fig. 6 because some $\Delta\omega, \Delta 2\theta$ points which receive no (or little) intensity for a particular value of w_2, owing to the source-size limitation on the positive-x side, can get some (or more) intensity for a larger value of w_2 owing to the possibility of greater depths of penetration. However, if a given $\Delta\omega, \Delta 2\theta$ point has no (or little) intensity due to the source-size limitation on the negative-x side, increasing w_2 will not provide any (or more) intensity. Hence the fact that the two-dimensional distributions lose some of their 'symmetry' for non-zero w_2.

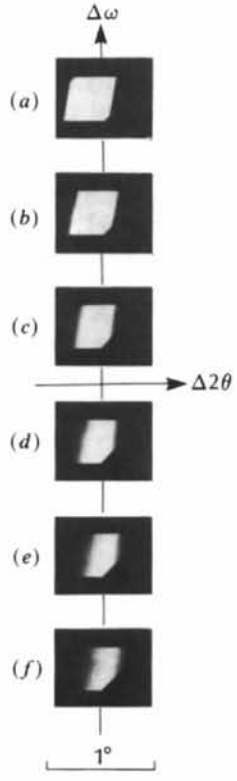

Fig. 7. Calculated $\Delta\omega, \Delta 2\theta$ intensity distributions for $t = 1{\cdot}0$, including the effects of depth of penetration. The values of w_2 are (*a*) 0·0, (*b*) 0·1, (*c*) 0·2, (*d*) 0·3, (*e*) 0·4 and (*f*) 3·0 mm. The value of Δz is 1 μm, and $\chi(\theta-\theta_M) = 2\exp[-16\ln 2(\theta-\theta_M)^2]+8\ \text{cm}^{-1}$ ($\theta-\theta_M$ in degrees).

In order to compare the positions of the two-dimensional intensity distributions of Fig. 7 in $\Delta\omega, \Delta 2\theta$ space it is useful to remember that the coordinates of the point (of non-zero intensity) where the $\Delta\omega$ value is minimum and the associated $\Delta 2\theta$ value is maximum (*i.e.* the 'bottom right corner') remain constant throughout Fig. 7. In Fig. 7(*a*) the origin ($\Delta\omega = \Delta 2\theta = 0$) is in the 'centre' of the intensity distribution, as it is for Figs. 2, 3, 4 and 5. This is not the case for Figs. 7(*b*) to (*f*), the 'centre' being progressively more to the right of the origin as w_2 increases. In general terms, the intensity at the points with lower $\Delta 2\theta$ values is not decreasing as w_2 increases in Fig. 7, but the intensity at points of higher $\Delta 2\theta$ is increasing relative to them.

It is apparent from the preceding discussion that we are treating the two-dimensional intensity distribution, $I(\Delta\omega, \Delta 2\theta)$, as the sum of two-dimensional intensity distributions, $I_z(\Delta\omega, \Delta 2\theta)$, from different depths of penetration into M:

$$I(\Delta\omega, \Delta 2\theta) = \sum_{z=0}^{w_2} I_z(\Delta\omega, \Delta 2\theta). \qquad (24)$$

This approach is clearly only an approximation to the true situation, but if Δz is chosen sensibly and $\chi(\theta-\theta_M)$ is realistic (*e.g.* Calvert, Killean & Mathieson, 1976; Mathieson, 1985*a*) the results should represent a considerable improvement, when depth of penetration is important, in comparison with ignoring the effect.

Fig. 8 displays the calculated $\Delta\omega, \Delta 2\theta$ distributions corresponding to those in Fig. 7 but for specific regions of z, namely, (*a*) [0·0, 0·1), (*b*) [0·1, 0·2), (*c*) [0·2, 0·3), (*d*) [0·3, 0·4), (*e*) [0·4, 0·5), (*f*) [0·5, 0·6), (*g*) [0·6, 0·7) and (*h*) [0·7, 0·8) mm. The value of Δz used was as for Fig. 7, *i.e.* 1 μm. The distributions in Fig. 8 have been displayed in such a way that the maximum intensity is given the 'whitest grey level', as are all the distributions presented in this paper. If we consider a scale on which the maximum intensity in Fig. 7(*f*) is given the value 10·0, then the maximum intensities for Figs. 8(*a*) to (*h*) are 3·7, 2·6, 1·9, 1·3, 0·9, 0·7, 0·5 and 0·2 respectively. We note that the sum of these values, 11·8, is greater than 10·0 because the maximum intensities occur at different positions in $\Delta\omega, \Delta 2\theta$ space (see preceding discussion). If the appropriate distributions in Fig. 8 are added together, with the correct weighting applied, those in Fig. 7 will be formed, *e.g.* Fig. 7(*d*) can be formed from Fig. 8(*a*) (×3·7/10·0), Fig. 8(*b*) (×2·6/10·0) and Fig. 8(*c*) (×1·9/10·0), on a relative scale. [Fig. 7(*f*) can be formed from just the distributions in Fig. 8, since there is no intensity arising from any depths of penetration larger than 0·78 mm in this case.]

The structure within the two-dimensional distributions of Figs. 7 and 8 is affected by the choice of

$\chi(\theta-\theta_M)$. Fig. 9 shows calculated $\Delta\omega$, $\Delta 2\theta$ distributions for $t=1{\cdot}5$, with the same parameter values as for Fig. 7 (with $w_2=0{\cdot}5$ mm), but with $\chi(\theta-\theta_M)$ multiplied by (*a*) 0·25, (*b*) 1·0, (*c*) 2·0, (*d*) 5·0, (*e*) 10·0 and (*f*) 1000·0. We see that as $\chi(\theta-\theta_M)\to\infty$, therefore eliminating the depth-of-penetration effect, the $\Delta\omega$, $\Delta 2\theta$ distribution tends to that expected from the earlier analyses. The FWHM of $\chi(\theta-\theta_M)$ will also affect the structure within the $\Delta\omega$, $\Delta 2\theta$ distributions.

5. Comparison with experiment

A high-resolution double-axis X-ray diffractometer has been used to collect several $\Delta\omega$, $\Delta 2\theta$ intensity distributions. The first (monochromator) axis can be varied (using a microcomputer-controlled stepping motor) in steps of approximately 7·5″, the second (specimen) axis can be similarly varied, in steps of approximately 0·5″. A scintillation detector can be rotated (independently) about the specimen axis in steps of approximately 0·5″. Both axes support motorized goniometer heads which are remotely controlled, and provide fine translational and angular adjustment of the two crystals.

The experimental arrangement, essentially that depicted in Fig. 1, has a fine-focus Cu X-ray tube disposed so that the effective source size is 0·4 mm (vertically) × 0·8 mm (w_1). This tube was run at generator settings of 45 kV and 26 mA, and the incident-beam collimation was provided by a 1·5 mm diameter hole just beyond the tube housing. The source-to-monochromator distance, d_1, is 10 cm. The monochromator used was pyrolytic graphite (ZYA: nominal mosaic spread of 0·4 ± 0·1°) of approximate dimensions 12·5 mm (vertically) × 24·5 mm (horizontally, *i.e.* in the diffraction plane) × 0·9 mm (thickness w_2). The monochromator was set for the peak of the 006 Cu $K\bar{\alpha}$ reflection, so that $d_M=1{\cdot}12$ Å and $\theta_M=43{\cdot}5°$. The monochromator-to-specimen distance, d_2, is 6·5 cm. The specimens used were Si wafers of (100), (110) and (111) orientation, and a narrow (vertical) slit was placed just before the specimen. The specimen reflections considered (all symmetric) were 111 ($\theta_S=14{\cdot}2°$; $t=0{\cdot}27$), 220 ($\theta_S=23{\cdot}7°$; $t=0{\cdot}46$), 400 ($\theta_S=34{\cdot}6°$; $t=0{\cdot}73$) and 333 ($\theta_S=47{\cdot}5°$; $t=1{\cdot}15$). The detector-slit width, w_3, was 0·1 mm, and placed 19 cm (d_3) from the specimen, *i.e.* the slit subtends an angle of approximately 0·03° at *S*.

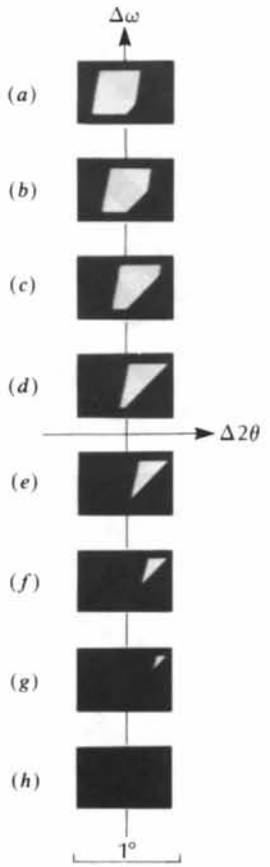

Fig. 8. Calculated $\Delta\omega$, $\Delta 2\theta$ intensity distributions corresponding to those in Fig. 7, but for the following regions of *z*: (*a*) [0·0, 0·1), (*b*) [0·1, 0·2), (*c*) [0·2, 0·3), (*d*) [0·3, 0·4), (*e*) [0·4, 0·5), (*f*) [0·5, 0·6), (*g*) [0·6, 0·7) and (*h*) [0·7, 0·8) mm.

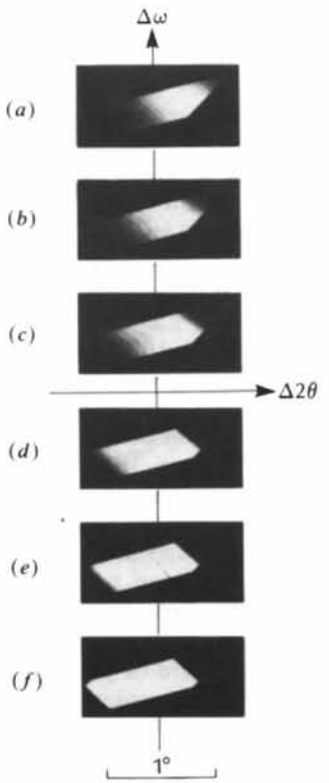

Fig. 9. Calculated $\Delta\omega$, $\Delta 2\theta$ intensity distributions for $t=1{\cdot}5$, $w_2=0{\cdot}5$ mm, and with $\chi(\theta-\theta_M)$ from Fig. 7 multiplied by (*a*) 0·25, (*b*) 1·0, (*c*) 2·0, (*d*) 5·0, (*e*) 10·0 and (*f*) 1000·0.

The choice of parameter values for the experimental arrangement described above (in particular, w_1, d_1, d_2, θ_M, λ_0 and an appropriate μ_M width) was influenced by a desire to ensure that both the $K\alpha_1$ and $K\alpha_2$ peaks could be seen in the $\Delta\omega$, $\Delta 2\theta$ intensity distributions. If we ignore, for a moment, the depth-of-penetration effect, then, for $\Delta = 0$, the source points for Cu $K\alpha_1$ and Cu $K\alpha_2$ are separated by approximately $w_1/2$, for the parameter values chosen here [see also Fig. 3 of Mathieson (1985*a*)]. It was also deemed necessary that the accessible values of t span a reasonable range [especially in the $(+, -)$ setting]. [For this experiment, the lower limit on t was set by the minimum θ_S value available (that for Si 111) and the upper limit was set by mechanical constraints on the diffractometer.]

In calculating the $\Delta\omega$,$\Delta 2\theta$ intensity distributions for the experimental arrangement described above (to compare with the measurements), the only parameters which are not already completely determined are λ_0 and those used to describe the functional form of μ_M. The functional form of σ is taken to be trapezoidal (*e.g.* Alexander & Smith, 1962; Stevenson, Mathieson & White, 1986), centred on $x = 0$, with the ratio of the widths at the base (w_1) and top being 5/3, a suitable choice for standard X-ray tubes. The functional form of λ is taken to be the sum of two Lorentzians (*e.g.* Hoyt, 1932), the first (second), for Cu $K\alpha_1$ (Cu $K\alpha_2$), centred on 1·54051 (1·54434) Å and having a FWHM of 0·00058 (0·00077) Å (Compton & Allison, 1935). The ratio of the peak heights for the two Lorentzians is such that the areas under the peaks are in the ratio 2:1 (Cu $K\alpha_1$:Cu $K\alpha_2$). The functional form of $\chi(\theta - \theta_M)$ is taken to be a Gaussian of height 1·8 cm^{-1} and FWHM 0·5° sitting on a base level of 9·2 cm^{-1} (Calvert, Killean & Mathieson, 1975, 1976) and $\Delta z = 1$ μm. The calculations presented in this section will include a numerical convolution with δ (see § 2).

The value of λ_0 used in this section is 1·54051 Å (Cu $K\alpha_1$) and the functional form of μ_M was taken to be the sum of two Gaussians of FWHM 0·2°, the first centred on $\Delta = 0°$, and the second centred on $\Delta = -0{\cdot}25°$ with 30% of the peak height of the first Gaussian. These parameter values are by no means 'fitted' but have been chosen to improve the agreement between the observed and calculated $\Delta\omega$, $\Delta 2\theta$ distributions. The selection of λ_0 affects, in particular, the ratio of the Cu $K\alpha_1$ and Cu $K\alpha_2$ intensities (due primarily to the *relatively* small source in the present case). The functional form of μ_M is consistent with the presence of some fragmentation (*e.g.* Mathieson, 1982).

Fig. 10 shows the (i) observed and (ii) calculated two-dimensional intensity distributions for the experimental arrangement described in this section. For the $(+, -)$ setting Fig. 10 displays the (*a*) 111, (*b*) 220, (*c*) 400 and (*d*) 333 reflections, and for the $(+, +)$ setting, (*e*) 400, (*f*) 220 and (*g*) 111 reflections. The calculated intensity distributions were obtained using points on a square grid of size 0·0139° (50″) in $\Delta\omega$ and $\Delta 2\theta$ (the same increment as was used for the measurements). (All other calculations in this paper have used a square grid of size 0·005° in $\Delta\omega$ and $\Delta 2\theta$.) The plots in Fig. 10 are presented on a logarithmic scale for clarity (all other plots have been on a linear scale).

The agreement between the observed and calculated $\Delta\omega$, $\Delta 2\theta$ distributions in Fig. 10 is excellent. This agreement might be improved further by systematically varying certain parameters (*e.g.* λ_0, and those associated with μ_M). It would also be instructive to reduce the grid size in $\Delta\omega$, $\Delta 2\theta$ space, for both observed and calculated distributions, if measurement and computer time, respectively, permitted. It should be emphasized that the only parameter which is altered in Figs. 10(*a*)(ii) to (*g*)(ii) is θ_S.

The size of the pyrolytic graphite monochromator, along y, is effectively infinite in the present case. The range of y values used for the reflections in Fig. 10 is (−3·62, 3·14) mm [(−2·31, 3·14) mm if depth-of-

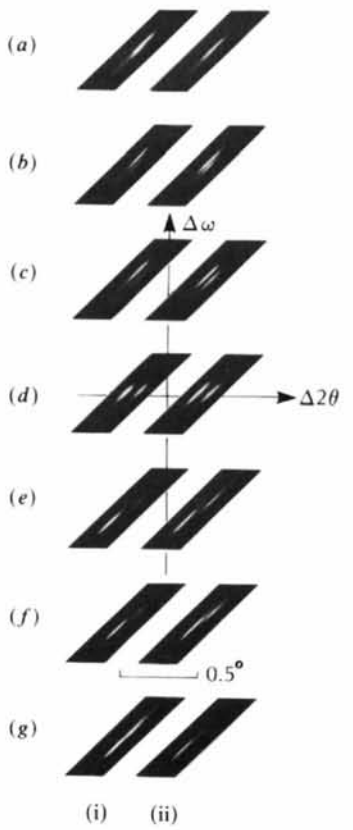

Fig. 10. The (i) observed and (ii) calculated $\Delta\omega$, $\Delta 2\theta$ intensity distributions for the experimental arrangement described in § 5. The $(+, -)$ setting is represented by the (*a*) 111, (*b*) 220, (*c*) 400 and (*d*) 333 reflections for different Si specimens, and the $(+, +)$ setting by the (*e*) 400, (*f*) 220 and (*g*) 111 reflections.

penetration effects are ignored]. The thickness of this monochromator is such that approximately 24% of the incident beam depicted in Fig. 1 will go all the way through the monochromator [for $\theta_M = 43{\cdot}5°$, $w_2 = 0{\cdot}9$ mm and $\chi(0) = 11$ cm^{-1}].

It is apparent that a full assessment of the foregoing theoretical treatment of $\Delta\omega, \Delta 2\theta$ intensity distributions would benefit from further comparisons with experiment. In particular, cases where more extensive wavelength bands are present (*e.g.* neutron or white-beam X-ray experiments) would facilitate such an assessment.

6. Discussion

The main aim of this paper has been to provide a systematic study of the form of $\Delta\omega, \Delta 2\theta$ intensity distributions for the case of crystal-monochromated X-radiation and a small specimen crystal. This is not only of interest in itself, and in respect of the advances that have been made in the resolution obtainable from linear position-sensitive detectors, but is also particularly relevant for the determination of one-dimensional intensity profiles and integrated intensities in a reasonable and consistent manner. Mathieson & Stevenson (1986*b*) have discussed 'counter' and 'film' profiles, and their relationship to the $\Delta\omega, \Delta 2\theta$ distribution. The $\Delta\omega, \Delta 2\theta$ technique is very instructive when decisions concerning appropriate scan ranges and detector-aperture sizes for truncating reflections in the course of a routine data collection have to be made (Mathieson, 1983, 1984*b*, 1985*b*).

The discussion presented in this paper has been in terms of the ω-scan mode, the results for other scan modes (ω/θ and $\omega/2\theta$ in particular) being derivable quite straightforwardly, as stated in § 1. For example, λ is constant along lines of gradient ∞ for the ω/θ scan mode (*i.e.* along lines parallel to the $\Delta\omega$ axis) and along lines of gradient -1 for the $\omega/2\theta$ scan mode, in $\Delta\omega, \Delta 2\theta$ space. Δ is constant along lines of gradient $(t \pm 1)/t$ for the ω/θ scan mode and $-(1 \pm t)$ for the $\omega/2\theta$ scan mode.

The approach used here to determine the form of the $\Delta\omega, \Delta 2\theta$ distributions is quite flexible and lends itself to modification. For example, one could readily include the effects of additional collimators and slits, or perhaps Soller slits, and so on, in the experimental arrangement. This might prove particularly useful when applying the theory to other radiations, *e.g.* neutrons or γ-rays. It is also possible to have an inhomogeneous mosaic spread associated with the monochromator, if appropriate. The extension of the theory to large and/or imperfect specimen crystals will be treated elsewhere.

It is a great pleasure to thank Professor A. McL. Mathieson for his interest, encouragement and input throughout the course of this work, and for reading and discussing the manuscript.

References

ALEXANDER, L. E. & SMITH, G. S. (1962). *Acta Cryst.* **15**, 983-1004.
CALVERT, L. D., KILLEAN, R. C. G. & MATHIESON, A. MCL. (1975). *Acta Cryst.* A**31**, 855-856.
CALVERT, L. D., KILLEAN, R. C. G. & MATHIESON, A. MCL. (1976). *Acta Cryst.* A**32**, 648-652.
COMPTON, A. H. & ALLISON, S. K. (1935). *X-rays in Theory and Experiment.* New York: Van Nostrand.
HOYT, A. (1932). *Phys. Rev.* **40**, 477-483.
MATHIESON, A. MCL. (1968). *Rev. Sci. Instrum.* **39**, 1834-1837.
MATHIESON, A. MCL. (1982). *Acta Cryst.* A**38**, 378-387.
MATHIESON, A. MCL. (1983). *Aust. J. Phys.* **36**, 79-83.
MATHIESON, A. MCL. (1984*a*). *J. Appl. Cryst.* **17**, 207-209.
MATHIESON, A. MCL. (1984*b*). *Aust. J. Phys.* **37**, 55-61.
MATHIESON, A. MCL. (1984*c*). *Acta Cryst.* A**40**, 355-363.
MATHIESON, A. MCL. (1985*a*). *Acta Cryst.* A**41**, 309-316. Erratum: *Acta Cryst.* (1986). A**42**, 287.
MATHIESON, A. MCL. (1985*b*). *J. Appl. Cryst.* **18**, 506-508.
MATHIESON, A. MCL. (1985*c*). *Acta Cryst.* A**41**, 603-605.
MATHIESON, A. MCL. (1988*a*). *Acta Cryst.* A**44**, 239-243.
MATHIESON, A. MCL. (1988*b*). *Acta Cryst.* A**44**, 1036-1042.
MATHIESON, A. MCL. & STEVENSON, A. W. (1984). *Aust. J. Phys.* **37**, 657-665.
MATHIESON, A. MCL. & STEVENSON, A. W. (1985). *Acta Cryst.* A**41**, 290-296.
MATHIESON, A. MCL. & STEVENSON, A. W. (1986*a*). *Acta Cryst.* A**42**, 223-230.
MATHIESON, A. MCL. & STEVENSON, A. W. (1986*b*). *Acta Cryst.* A**42**, 435-441.
STEVENSON, A. W. (1989). In preparation.
STEVENSON, A. W., MATHIESON, A. MCL. & WHITE, A. H. (1986). *J. Appl. Cryst.* **19**, 143.
WILKINS, S. W., CHADDERTON, L. T. & SMITH, T. F. (1983). *Acta Cryst.* A**39**, 792-800.